

Supermassive Black Hole Formation by Direct Collapse: Keeping Protogalactic Gas H₂–Free in Dark Matter Halos with Virial Temperatures $T_{\text{vir}} \gtrsim 10^4$ K

Cien Shang^{1*}, Greg L. Bryan² and Z. Haiman²

¹*Department of Physics, Columbia University, 538 West 120th Street, New York, NY 10027*

²*Department of Astronomy, Columbia University, 550 West 120th Street, New York, NY 10027*

9 September 2021

ABSTRACT

In the absence of H₂ molecules, the primordial gas in early dark matter halos with virial temperatures just above $T_{\text{vir}} \gtrsim 10^4$ K cools by collisional excitation of atomic H. Although it cools efficiently, this gas remains relatively hot, at a temperature near $T \sim 8000$ K, and consequently might be able to avoid fragmentation and collapse directly into a supermassive black hole (SMBH). In order for H₂–formation and cooling to be strongly suppressed, the gas must be irradiated by a sufficiently intense ultraviolet (UV) flux. We performed a suite of three–dimensional hydrodynamical adaptive mesh refinement (AMR) simulations of gas collapse in three different protogalactic halos with $T_{\text{vir}} \gtrsim 10^4$ K, irradiated by a UV flux with various intensities and spectra. We determined the critical specific intensity, J_{21}^{crit} , required to suppress H₂ cooling in each of the three halos. For a hard spectrum representative of metal–free stars, we find (in units of 10^{-21} erg s^{−1} Hz^{−1} sr^{−1} cm^{−2}) $10^4 < J_{21}^{\text{crit}} < 10^5$, while for a softer spectrum, which is characteristic of a normal stellar population, and for which H[−]–dissociation is important, we find $30 < J_{21}^{\text{crit}} < 300$. These values are a factor of 3–10 lower than previous estimates. We attribute the difference to the higher, more accurate H₂ collisional dissociation rate we adopted. The reduction in J_{21}^{crit} exponentially increases the number of rare halos exposed to super–critical radiation. When H₂ cooling is suppressed, gas collapse starts with a delay, but it ultimately proceeds more rapidly. The infall velocity is near the increased sound speed, and an object as massive as $M \sim 10^5$ M_⊙ may form at the center of these halos, compared to the $M \sim 10^2$ M_⊙ stars forming when H₂–cooling is efficient.

Key words: cosmology:theory – black holes physics – methods:numerical

1 INTRODUCTION

The discovery of very bright quasars, with luminosities $\geq 10^{47}$ erg s^{−1}, at $z \simeq 6$ in the Sloan Digital Sky Survey (SDSS) suggests that some SMBHs as massive as a few times 10^9 M_⊙ already existed when the universe was less than 1 Gyr old (see, e.g., Fan 2006 for a review). In principle, these large black hole (BH) masses, inferred from the apparent luminosities, could have been overestimated due to strong gravitational lensing and/or beaming. However, no obvious sign of either effect was found in the images or spectra of these quasars (Willott et al. 2003; Richards et al. 2004).

Explaining how SMBHs with masses in excess of

10^9 M_⊙ could assemble within 1 Gyr presents some challenges. Perhaps the most natural proposal is that they grow, by a combination of Eddington–limited accretion and mergers, from the stellar–mass seed BHs provided by the remnants of the first generation of massive, metal–free stars (e.g., Haiman & Loeb 2001). Indeed, the initial seed BHs, with masses of the order of their progenitor stars, ~ 100 M_⊙ (Abel et al. 2000, 2002; Bromm et al. 2002), are expected to be present very early (at redshifts prior to $z \gtrsim 10$). There are, however, a number of potential difficulties with this scenario. First, the early seeds must accrete near the Eddington rate for a Hubble time, without any prolonged interruption (Haiman & Loeb 2001), which requires that the BHs are continuously surrounded by dense gas (e.g. Turner 1991; Alvarez et al 2009). However, early seed BHs are expected to undergo frequent mergers, and the gravitational

* E-mail: cien@phys.columbia.edu, gbryan@astro.columbia.edu, zoltan@astro.columbia.edu

waves emitted during the BH mergers impart a strong recoil to the coalesced BHs (e.g. Pretorius 2005; Campanelli et al. 2006; Baker et al. 2006). The typical velocity of this gravitational kick is expected to exceed ~ 100 km/s, which is significantly higher than the escape velocity ($\lesssim 10$ km/s) from typical dark matter halos at $z \sim 10$. BHs are therefore easily ejected, or at least displaced from the dense nuclei of their host halos at high redshift, interrupting their accretion (Haiman 2004; Yoo & Miralda-Escudé 2004; Shapiro 2005; Volonteri & Rees 2006; Blecha & Loeb 2008; Tanaka & Haiman 2009). Even if such disruptive kicks are avoided (because mergers at early times may be rare and/or occur primarily between unequal-mass BHs; Volonteri & Rees 2006; Tanaka & Haiman 2009), there remain two fundamental difficulties. First, when the effects of photoheating and radiation pressure are included, the maximum allowed steady accretion rate is significantly reduced, at least in spherical symmetry (e.g. Milosavljevic et al. 2009a), suggesting that accretion must be intermittent, with a time-averaged rate well below the Eddington-limit (e.g. Ciotti & Ostriker 2001, 2007; Milosavljevic et al. 2009b). Second, models in which sufficient numbers of early BHs are able to accrete and grow to $10^9 M_\odot$ by $z \approx 6$ tend to overproduce the abundance of $\approx 10^6 M_\odot$ BHs by several orders of magnitude (compared to the abundance inferred from local observations). This requires a preferential suppression of BH growth in low-mass halos, plausibly due to negative feedback effects acting on these halos (Bromley et al. 2004; Tanaka & Haiman 2009).

An alternative way of assembling SMBHs is through more rapid (super-Eddington) accretion or collapse. In this family of models, primordial gas collapses directly into a BH as massive as $10^4 - 10^6 M_\odot$ (Oh & Haiman 2002 [hereafter OH02]; Bromm & Loeb 2003 [hereafter BL03]; Koushiappas et al. 2004; Lodato & Natarajan 2006; Spaans & Silk 2006; Begelman et al. 2006; Volonteri et al. 2008), possibly onto a pre-existing smaller seed BH (Volonteri & Rees 2005), or through the intermediate state of a very massive star (BL03). Such a head-start evades problems encountered by the models where SMBHs grow at the Eddington limit from stellar mass seeds. A necessary condition for such direct collapse models is that the collapsing gas avoid fragmentation; otherwise, normal Pop III stars would be produced.¹ At the density of $\sim 10^4 \text{ cm}^{-3}$ (the critical density for H_2 ; see below), the Jeans mass is $M_J \approx 10^6 M_\odot (T/10^4 \text{ K})^{3/2}$. The gas temperature T depends crucially on whether H_2 cooling is efficient: $T \approx 100$ K, achievable if H_2 cooling is efficient, would imply $M_J \approx 10^3 M_\odot$, so that PopIII stars might form, whereas $T \approx 10^4$ K, expected in the absence of H_2 , would yield $M_J \approx 10^6 M_\odot$, suggesting that direct collapse into a $M \approx 10^6 M_\odot$ SMBH may be feasible (OH02).

Numerical simulations have indeed shown that fragmentation is inefficient when H_2 cooling is absent (BL03; Regan & Haehnelt 2009a, 2009b). However, in most models, the absence of H_2 was assumed, rather than derived. The notable exceptions are Spaans & Silk (2006), whose model does not

require any explicit H_2 destruction², and BL03, who performed simulations with an H_2 -photodissociating Lyman-Werner background. The absence of H_2 molecules from protogalactic halo gas can be justified by a sufficiently intense UV radiation, either in the Lyman-Werner bands, directly photo-dissociating H_2 (near a photon energy of $\sim 12\text{eV}$) or photo-dissociating the intermediary H^- (photon energies $\gtrsim 0.76\text{eV}$). The relevant criterion is that the photodissociation timescale is shorter than the H_2 -formation timescale; since generically, $t_{\text{diss}} \propto J$ and $t_{\text{form}} \propto \rho$, the condition $t_{\text{diss}} = t_{\text{form}}$ yields a critical flux that increases linearly with density, $J^{\text{crit}} \propto \rho$. In “minihalos”, with virial temperatures $T_{\text{vir}} < 10^4 \text{ K}$, the gas cannot cool in the absence of H_2 , the densities remain low ($\sim 1 \text{ cm}^{-3}$; e.g. Mesinger et al. 2006) and H_2 can be dissociated even by a relatively feeble UV flux. The critical value has been found to be $J_{21} \sim 0.1$ (Haiman et al. 1997; Machacek et al. 2001, 2003; Mesinger et al. 2006, 2008; Wise & Abel 2007; O’Shea & Norman 2008; here and in the rest of the paper, J_{21} denotes the specific intensity just below 13.6eV , in the usual units of $10^{-21} \text{ erg cm}^{-2} \text{ sr}^{-1} \text{ s}^{-1} \text{ Hz}^{-1}$). This value is much smaller than the expected level of the cosmic UV background in the Lyman-Werner bands near reionization (BL03)

$$J_{\text{bg}} \approx \frac{1}{f_{\text{esc}}} \frac{hc}{4\pi} \frac{N_\gamma Y_{\text{H}} \rho_{\text{b}}}{m_{\text{p}}} \quad (1)$$

or

$$J_{21} \approx 40 \left(\frac{N_\gamma}{10} \right) \left(\frac{f_{\text{esc}}}{0.1} \right)^{-1} \left(\frac{1+z}{11} \right)^3, \quad (2)$$

where f_{esc} is the escape fraction of ionizing radiation, N_γ is the average number of photons needed to ionize a hydrogen atom, $Y_{\text{H}} = 0.76$ is the mass fraction of hydrogen, m_{p} is the proton mass, and ρ_{b} is the background baryon density with $\Omega_{\text{b}} h^2 = 0.023$.

The critical intensity J_{21}^{crit} in larger halos, with virial temperatures $T_{\text{vir}} \geq 10^4 \text{ K}$, however, is much higher (Omukai 2001, hereafter OM01; OH02; BL03). This is primarily because the gas in these halos can cool via excitations of atomic H and reach much higher densities, and because the H_2 molecules can then become self-shielding (OH02). In particular, for halos with $T_{\text{vir}} \sim 10^4 \text{ K}$, the value has been estimated in one-zone models to be $J_{21}^{\text{crit}} \approx 10^3 - 10^5$ (OM01). This range covers different assumed spectral shapes; in particular, a thermal spectrum with $T_* = 10^4 - 10^5 \text{ K}$ (OM01). Using three-dimensional smooth particle hydrodynamics (SPH) simulations, BL03 find $J_{21}^{\text{crit}} \gtrsim 10^5$ (for $T_* = 10^5 \text{ K}$) and $J_{21}^{\text{crit}} \lesssim 10^3$ (for $T_* = 10^4 \text{ K}$), in agreement with the one-zone results.

The UV background that illuminates collapsing $T_{\text{vir}} \approx 10^4 \text{ K}$ halos was likely established by the massive pop-III stars that had formed in previous generations of minihalos. In this case, the background spectrum is likely to be closer to the $T_* = 10^5 \text{ K}$ case, implying $J_{21}^{\text{crit}} \gtrsim 10^5$. Furthermore, the early minihalos are expected to be easily

¹ Another necessary condition is for the gas to lose angular momentum efficiently. Other than the angular momentum transfer occurring above the resolution of our simulations, this topic will not be addressed in the present paper. See, e.g. Begelman et al. (2006) for a discussion and for references.

² Spaans & Silk propose that over a relatively narrow range of densities and hydrogen column densities, the Ly α photons emitted by atomic H cooling are trapped within the collapsing gas – this prevents the temperature from falling below $\sim 8,000 \text{ K}$, and keeps the H_2 molecules collisionally dissociated.

self-ionized, with most of their ionizing radiation escaping into the intergalactic medium, i.e. $f_{\text{esc}} \approx 1$ (Kitayama et al. 2004; Whalen, Abel & Norman 2004). Equation 2 shows that, unless f_{esc} is much smaller, and/or N_γ is large ($f_{\text{esc}}/N_\gamma \lesssim 10^{-3}$), the mean cosmic background is unlikely to reach the required critical value. The background will have inevitable spatial fluctuations, and a very small fraction $f(J > J^{\text{crit}}_{21})$ of 10^4 K halos that have an unusually close and bright neighbor may still see a sufficiently high flux. Dijkstra et al. (2008) used a model for the three-dimensional spatial clustering of halos to estimate this fraction, and found $f(J > 10^3) \sim 10^{-6}$, with an exponential dependence of this result on J^{crit}_{21} .³

In this paper, we derive detailed estimates for J^{crit}_{21} based on a suite of 3D hydrodynamic simulations. Our motivation is two-fold. First a UV intensity that exceeds J^{crit}_{21} is crucial for the feasibility of direct SMBH formation models. Second, the existing estimates of J^{crit}_{21} significantly exceed the expected value of the mean cosmic background. If these estimates are correct, then $J > J^{\text{crit}}_{21}$ will be experienced only by those rare halos that probe the bright tail of the spatially fluctuating background J . In this case, even a small change in the value of J^{crit}_{21} can cause a large change in the expected number of halos that can form SMBHs by direct collapse.

Our paper adds to the earlier work of OM01, which estimated J^{crit}_{21} based on a one-zone model with a fixed, prescribed collapse dynamics, that could not address fragmentation, and to the results of BL03, who use three-dimensional simulations, but report only approximate upper and lower limits on J^{crit}_{21} for a single halo. In addition, we study the behavior of the collapsing gas in detail as a function of J_{21} , and obtain a rough estimate for the fluctuations in J^{crit}_{21} by following the collapse of three different halos. We also obtain a quantitative estimate of the final collapsed central massive object, based on the infall time-scales observed in each case.

The rest of this paper is organized as follows. In § 2, we describe the simulation setup in detail. In § 3, we present the range of J^{crit}_{21} values derived from the simulations, and explain the underlying physics using a one-zone model. We also estimate the fluctuations in J^{crit}_{21} . In § 4, we discuss the ultimate fate of the halos, for different values of J_{21} . Finally, we summarize the results and present the conclusion of this work in § 5.

2 NUMERICAL METHODOLOGY

We use the Eulerian adaptive mesh refinement (AMR) code Enzo, which has been tested extensively and is publicly available (Bryan 1999; Norman & Bryan 1999; O’Shea et al. 2004). Enzo uses an N-body particle-mesh solver to follow dark matter dynamics, and an Eulerian AMR method by

Berger & Colella (1989) to solve the hydrodynamical equations for an ideal gas. This combination allows for high dynamic range in gravitational physics and hydrodynamics. Nested grids are used whenever higher resolution is needed. At each new refinement level, a parent grid is replaced by a few smaller child grids.

The chemical composition of the gas is followed by solving the non-equilibrium evolution of nine species: H, H^+ , He, He^+ , He^{++} , H^- , H_2^+ , H_2 , and e^- (Abel et al. 1997; Abel et al. 2000). Our reaction network did not include HD or other molecules involving deuterium. This should make very little difference to our results, since HD cooling only becomes important for temperatures below a few hundred Kelvin (McGreer & Bryan 2008). The H_2 radiative cooling function of Galli & Palla (1998) is employed to follow the temperature of the gas.

A few modifications were made to the publicly available Enzo code. First, we added direct H^- photodissociation into chemistry solver,



As explained below, this reaction is important in determining the value of J^{crit}_{21} . Second, we included the self-shielding of H_2 in the LW bands when computing H_2 photodissociation rate. Specifically, the intensity in the LW band is multiplied by a self-shielding factor f_{sh} given by Draine & Bertoldi (1996),

$$f_{\text{sh}} = \min \left[1, \left(\frac{N_{H_2}}{10^{14} \text{cm}^{-2}} \right)^{-3/4} \right], \quad (4)$$

where N_{H_2} is the H_2 column density. Since N_{H_2} is a non-local quantity, it is computationally very expensive to obtain its exact value. To save computing time, we made the commonly used approximation,

$$N_{H_2} = f_{H_2} n_{\text{tot}} \lambda_J, \quad (5)$$

where f_{H_2} , n_{tot} and λ_J are the H_2 fraction by number, the total particle number density, and the Jeans length, respectively. With this approximation, N_{H_2} and f_{sh} can be computed from the local values of the temperature, density and H_2 fraction. We will quantify the accuracy of this approximation in § 3.5 below.

The simulation is set up in a comoving box of size $1 h^{-1}$ Mpc, assuming a standard Λ CDM model with the following parameter: $\Omega_{\text{DM}} = 0.233$, $\Omega_b = 0.0462$, $\Omega_\Lambda = 0.721$, $\sigma_8 = 0.817$, $n_s = 0.96$ and $h = 0.701$ (Komatsu et al. 2009). We first perform a preliminary run in order to identify halos suitable for detailed study. This run has a root grid with a resolution of 128^3 and no nested grids. Radiative cooling is turned off, so that the gas in the halos is unable to contract to high densities in this run. We evolved the simulation to $z = 10$, stopped it, and used the HOP halo finding algorithm (Eisenstein & Hut 1998) to identify dark matter halos in the output files. Three halos, which are labeled below as A, B and C, were chosen for high-resolution re-runs. All three of these were selected to have virial masses of a few $\times 10^7 M_\odot$ at a redshift of $z = 10$. In this paper, virial mass is defined to be the total mass, including both gas and dark matter components, inside a spherical averaged overdensity of 200 with respect to the critical density of the universe.

We generated a new set of initial conditions for the three

³ Alternatively, the critical value could be established by sources internal to the halo, e.g. by a vigorous phase of starburst (Omukai & Yoshii 2003) or by an accreting stellar seed BH (Volonteri & Rees 2005). However, having gone through star-formation already, the halo gas is unlikely to still be metal-free, and is then likely to fragment into low-mass stars, rather than collapsing directly into a SMBH (Omukai et al. 2008).

chosen halos. Three nested grids with twice finer resolution were added, so that the effective resolution of the innermost grid was 1024^3 , resulting in a dark matter particle mass of $86 M_\odot$. Radiative cooling was turned on in the re-runs, and the grid cells were adaptively refined based on the following three criteria: baryon mass, dark matter mass and Jeans length. According to the first two criteria, additional grids are added when the baryon (dark matter) mass in a grid cell exceeds 68 (683) solar mass, corresponding to 4 (8) times the initial mass in one grid cell (particle) in the most refined region. The third criterion ensures that the Jeans length is resolved by at least 4 grid cells, so that no artificial fragmentation would take place. In addition, to avoid numerical effects due to the finite mass of dark matter particles, the gravity of dark matter particles is smoothed at refinement level 13, which corresponds to a smoothing scale of $0.954/h$ (comoving) parsec. Each dark matter particle has a mass of $\sim 85 M_\odot$. We allow the simulations to proceed until a maximum refinement level of 18 is achieved, corresponding to a resolution of $0.0298/h$ (comoving) parsec, or about 800 AU (absolute).

For each of the three halos, we ran a series of simulations with different UV spectra and intensities. For the spectral shape, we adopted a Planck spectrum with a black-body temperature of either $T_* = 10^4$ K or $T_* = 10^5$ K (hereafter denoted by T4 and T5, respectively). The softer of these spectra is meant to approximate the mean spectrum of a normal stellar population, whereas the higher-temperature case is closer to the harder spectrum expected to be emitted by the first generation of massive, metal-free stars (Tumlinson & Shull 2000; Bromm, Kudritzki & Loeb 2001; Schaerer 2002). Using these two spectral types allows us to compare our results with previous work (OM01, BL03) which adopted the same spectral shapes. In Table 1 (2), we list the redshift (z_{col}), virial mass ($m_{\text{vir,col}}$) and central gas temperature (T_{cent}) in the halos when their cores collapse in the presence of type T4 (T5) UV background. Here, “core collapse” is simply defined as the time when the maximum refinement level (level 18) is reached. In practice, once the collapse starts, it proceeds very rapidly. As a result, the refinement level adopted for this definition makes little difference to our results, as long as it is chosen to be at level 13 or higher. We generally varied J_{21} by factors of 10, but included additional runs with $J_{21} = 3 \times 10^2$ for halos B and C in the T4 case in order to determine J_{21}^{crit} more precisely. The values for the $J_{21} = 10^3$ case for halo C are missing from Table 1, because the halo moved out of the refinement region before it collapsed in this run. This occurred because of the late collapse redshift for this halo (recall that halos were selected at $z = 10$). We could have rerun the simulation with a larger refined region, but this was unnecessary because the $J_{21} = 3 \times 10^2$ run was sufficient for determining J_{21}^{crit} .

3 THE CRITICAL VALUE OF J_{21}

3.1 Results from Three-Dimensional Simulations

Based on the central gas temperatures (T_{cent}) listed in Tables 1 and 2, the halos can be grouped unambiguously into two categories: “cool” halos and “hot” halos. The “cool”

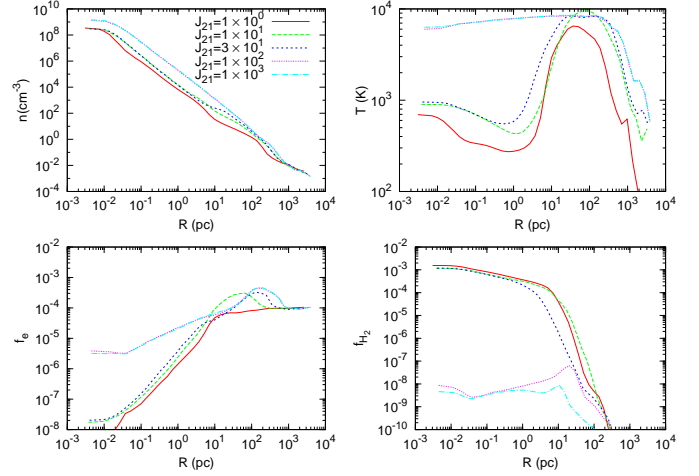


Figure 1. Spherically averaged profiles of the particle density, gas temperature, e^- fraction and H_2 fraction in halo A, for different values of the intensity J_{21} of a type T4 background.

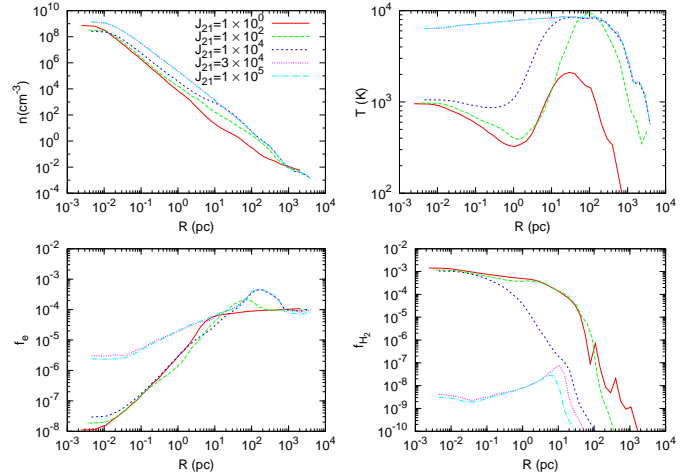


Figure 2. Same as Figure 1 except for type T5 backgrounds.

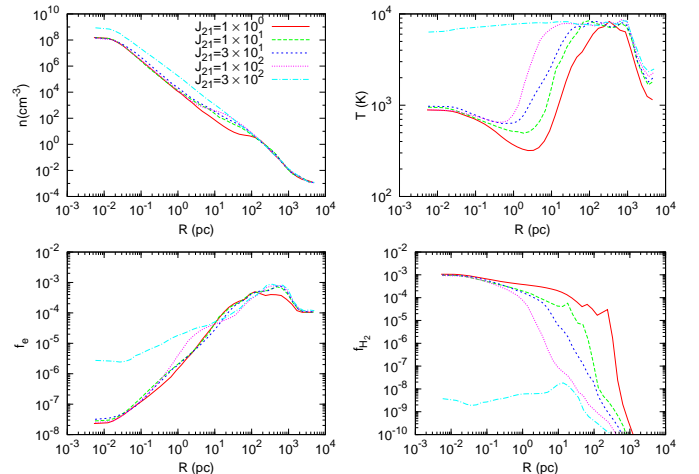


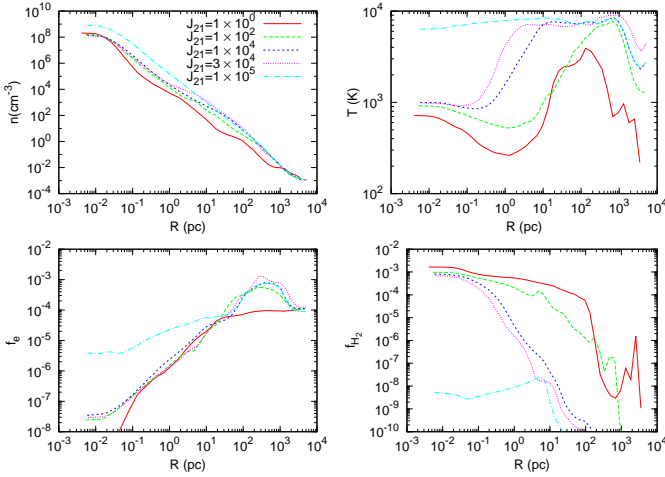
Figure 3. Same as Figure 1 except for Halo C.

Table 1. Redshift (z_{col}), virial mass ($m_{\text{vir,col}}$) and central gas temperature (T_{cent}) of the halos when their cores collapse in the presence of a $T_* = 10^4$ K black-body (“T4”) UV background.

J_{21}	Halo A			z_{col}	Halo B			z_{col}	Halo C		
	z_{col}	$m_{\text{vir,col}}(\text{M}_{\odot})$	$T_{\text{cent}}(\text{K})$		$m_{\text{vir,col}}(\text{M}_{\odot})$	$T_{\text{cent}}(\text{K})$	$m_{\text{vir,col}}(\text{M}_{\odot})$		$T_{\text{cent}}(\text{K})$		
1×10^0	15.47	6.87×10^6	695.18	9.63	6.76×10^7	879.89	8.48	7.55×10^7	888.19		
1×10^1	12.22	2.49×10^7	900.80	9.53	6.94×10^7	778.41	7.89	8.85×10^7	951.86		
3×10^1	11.41	3.16×10^7	955.52	9.11	8.80×10^7	957.48	7.81	9.08×10^7	974.82		
1×10^2	10.02	5.33×10^7	5985.60	8.93	9.59×10^7	807.96	7.65	9.77×10^7	890.45		
3×10^2	-	-	-	8.91	9.63×10^7	6356.30	7.61	1.04×10^8	6334.20		
1×10^3	9.96	5.43×10^7	6291.10	8.90	9.67×10^7	6395.90	-	-	-		

Table 2. Same as Table 1, but for a $T_* = 10^5$ K black-body (“T5”) UV background.

J_{21}	Halo A			z_{col}	Halo B			z_{col}	Halo C	
	z_{col}	$m_{\text{vir,col}}(\text{M}_{\odot})$	$T_{\text{cent}}(\text{K})$		$m_{\text{vir,col}}(\text{M}_{\odot})$	$T_{\text{cent}}(\text{K})$	z_{col}		$m_{\text{vir,col}}(\text{M}_{\odot})$	$T_{\text{cent}}(\text{K})$
1×10^0	19.75	1.29×10^6	955.27	19.57	5.70×10^5	769.93	11.23	7.97×10^6	718.78	
1×10^2	12.27	2.45×10^7	973.94	9.65	6.74×10^7	845.56	8.30	7.89×10^7	918.84	
1×10^4	10.03	5.31×10^7	1055.20	8.94	9.56×10^7	963.06	7.49	1.08×10^8	998.76	
3×10^4	9.99	5.39×10^7	6329.20	8.92	9.65×10^7	1064.40	7.07	1.23×10^8	988.36	
1×10^5	9.93	5.49×10^7	6368.90	8.90	9.68×10^7	6446.30	7.48	1.09×10^8	6322.90	


Figure 4. Same as Figure 3 except for type T5 backgrounds.

halos all have central temperatures near ~ 1000 K, whereas the “hot” halos all have central temperatures near ~ 6000 K. To see the differences between these two categories more clearly, we show in Figures 1 - 4 the spherically averaged profiles of the particle density, gas temperature, e^- fraction and H_2 fraction in halos A and C, for different values of J_{21} , and in the presence of type T4 and T5 UV backgrounds. The profiles of halo B are not shown because they are very similar to those of halo C. All profiles are shown at the time of collapse at z_{coll} . The collapse is delayed significantly as the intensity of the background is increased (see Tables 1 and 2), so that the curves shown in each panel reflect conditions at significantly different redshifts.

Consistent with the values in Tables 1 and 2, these figures show that central temperatures are very different for “hot” and “cool” halos. However, the temperature profiles at

large radii are actually similar in the cases where $J_{21} \geq 10$. As the gas falls in, the temperature first rises due to virialization shocks, and stays at ~ 8000 K because of atomic cooling. The clear differences arise around $R \sim 10$ pc, where the “cool” halos start to cool via H_2 , while the “hot” halos stay hot. As the figures show, $R \sim 10$ pc corresponds to a density of $n \sim 10^3 \text{ cm}^{-3}$. The conditions at this density are crucial in determining the value of J_{21}^{crit} . In particular, the difference in the temperature profiles is clearly induced by the difference in the H_2 fractions. As the bottom right panel of each of Figures 1 - 4 shows, the H_2 fractions increase with decreasing radii in the “cool” halos. In the “hot” halos, the fractions increase with decreasing radii outside $R \sim 10$ pc, but the fraction stays constant, at the low level of $\sim 10^{-8}$, inside this radius. There are also clear differences in e^- fraction profiles: the cores of the “hot” halos have a much larger electron fraction ($\sim 10^{-5}$), whereas in the cores of the “cool” halos, the electrons are depleted. Finally, although the density profiles are overall quite similar, the gas densities reached within the inner ~ 10 pc in the “hot” halos are noticeably higher than in the “cool” halos.

As we will discuss in more detail in § 4 below, during the process of quasi-static contraction, the density and temperature adjust so that the cooling, sound crossing, and dynamical time scales are all approximately equal ($t_{\text{cool}} \approx t_{\text{cross}} \approx t_{\text{ff}}$). From the condition $t_{\text{cross}} \approx t_{\text{ff}}$, we find $nR^2 \propto T$ (see equation 16 below), which explains why the density is higher when temperature is higher at a given radius. Within $R \sim 10$ pc, the e^- fractions in “hot” halos have a much shallower slope than in “cool” halos. This is because the main reactions determining the electron fraction (reactions 1 and 4 in the Appendix) are highly temperature sensitive – in particular, recombinations (reaction 4) are exponentially more rapid at lower temperatures, and the gas is therefore much more fully recombined in the “cool” halos.

Table 3. J_{21}^{crit} for the three different halos (A, B, and C), and for the two different UV background spectra (T4 and T5).

	Halo A	Halo B	Halo C	One-zone
T4	$3 \times 10^1 - 10^2$	$10^2 - 3 \times 10^2$	$10^2 - 3 \times 10^2$	3.9×10^1
T5	$10^4 - 3 \times 10^4$	$3 \times 10^4 - 10^5$	$3 \times 10^4 - 10^5$	1.2×10^4

It is worth noting that in the case of $J_{21} = 1$ and type T5 UV background, the halo gas is able to collapse before the halo potential grows deep enough to reach a virial temperature of ~ 8000 K, where atomic cooling becomes important. Effectively, at this low UV background, the halos are “minihalos”, whose properties are fully determined by H_2 cooling. This causes a “break” in the properties of halos, such as their mass and collapse redshift, between $J_{21} = 1$ and $J_{21} = 10$. Such a “break” was also seen in O’Shea & Norman (2008), but at $J_{21} \sim 0.1$. The fact that this break occurs at a higher J_{21} in our simulations is not surprising, since we include self-shielding, which was ignored in O’Shea & Norman (2008).

Finally, we note that even in the cases with higher values of J_{21} , when the collapse is delayed, and the dark matter halo potentials grow somewhat deeper, the effective virial temperature of the halos we examined are still only marginally (if at all) above 10^4 K. Indeed, Figures 1 - 4 show that the gas in the simulated halos is never fully collisionally ionized – the highest free electron fraction reached is only 10^{-3} . This regime differs from the common assumption that “second generation” halos are collisionally ionized (e.g. OH02). In the strict absence of any H_2 cooling, the shocks that occur in more massive halos could, of course, eventually produce full ionization. However, prior to building up this higher mass, every halo must go through the “marginal” stage where its effective virial temperature is close to, but just above, $T_{\text{vir}} \approx 10^4$ K. As our results show, the gas at this stage can already cool efficiently via excitations of atomic H. Therefore, we expect that halos that reach virial temperatures significantly above $\approx 10^4$ K and become fully ionized, but still consist of pure atomic H (and He), will be exceedingly rare.

Because each of our runs produce a collapsed halo that belongs unambiguously either to the “cool” or “hot” category, we simply define J_{21}^{crit} as the value that divides these two regimes. Our suite of simulations is then sufficient to determine J_{21}^{crit} to within a factor ~ 3 for each of the three halos, and for the two types of UV spectra. The results are listed in Table 3.

There are two interesting new points that can be concluded from the J_{21}^{crit} values in Table 3. First, the ranges of J_{21}^{crit} we found are smaller than previously estimated. Previous studies (OM01; Omukai et al. 2008) found $J_{21}^{\text{crit}} \approx 10^3$ for the type T4 spectrum and $\sim 3 \times 10^5$ for the type T5 spectrum. The upper and lower limits of $\lesssim 10^3$ and $\gtrsim 10^5$, reported from SPH simulations by BL03 for these two types of spectra, are consistent with the above values. These values, however, are a factor of ~ 10 larger than our results for halo A, and a factor of ~ 3 larger than for halos B and C. Second, even with our crude sampling of J values, we see a

“scatter” in J_{21}^{crit} : the critical flux is a factor of ~ 3 lower for halo A than for halos B and C, despite the similar masses and collapse redshifts of these halos.

The fact that we find J_{21}^{crit} values that are smaller than previously estimated is particularly important, because the critical UV fluxes are high compared to the expected level of the cosmic UV background at high redshifts. As noted above, however, the background will inevitably have spatial fluctuations, and a small fraction of halos may still see a sufficiently high flux. Dijkstra et al. (2008) used a model for the three-dimensional spatial clustering of halos to estimate the probability distribution function (PDF) of the background LW flux J_{bg} , as sampled by DM halos with $T_{\text{vir}} \approx 10^4$ K. Their results show that the interesting range of J_{21}^{crit} samples the bright, steeply falling tail of the flux PDF. In particular, in their Figure 2, Dijkstra et al. (2008), show the fraction $f(> J_{21}^{\text{crit}})$ of halos exposed to a flux above a given J_{21}^{crit} . This fraction is very sensitive to J_{21}^{crit} : for $J_{21}^{\text{crit}} \gtrsim 10^4$, the PDF drops to negligibly low values ($f \lesssim 10^{-8}$); for $J_{21}^{\text{crit}} = 10^3$, $f \sim 10^{-6}$, whereas for $J_{21}^{\text{crit}} = 10^2$, $f \sim 10^{-3}$. This implies that the 10-fold decrease we find in the value of J_{21}^{crit} increases the number of candidate DM halos, where direct SMBH formation may be feasible, by a factor of $\approx 10^3$.

3.2 Results from One-Zone Models

In order to understand the above results, we performed one-zone calculations similar to those in OM01. The chemical reaction and cooling rates are set to be the same as in the Enzo runs, but the gas density is assumed to have a single value that follows a fixed prescribed evolution. The list of chemical reactions we used, and their rates, are shown in the Appendix. In this model, the dark matter and the baryons start their collapse at the turnaround redshift, which is set to be $z = 17$. At this redshift, zero initial velocities are assumed. The subsequent evolution of the dark matter density is computed using the spherical collapse model, up to the time of virialization, after which it is assumed to stay constant at the virial density. The evolution of the baryonic component is followed using the equation,

$$\frac{d\rho_b}{dt} = \frac{d\rho_b}{t_{\text{ff}}}, \quad (6)$$

where ρ_b is the baryonic density, and $t_{\text{ff}} = \sqrt{3\pi/32G\rho}$ is the dynamical (free-fall) time. The thermal evolution is described the following equation,

$$\frac{de}{dt} = -p \frac{d}{dt} \left(\frac{1}{\rho_b} \right) - \frac{\Lambda_{\text{net}}}{\rho_b}, \quad (7)$$

where e is the internal energy per unit baryonic mass, p is the gas pressure, and Λ_{net} is the net cooling rate computed using cooling function by Galli and Palla (1998). The internal energy density is computed from

$$e = \frac{1}{\gamma - 1} \frac{k_B T}{\mu m_H}, \quad (8)$$

where $\gamma = 5/3$ is the adiabatic index, k_B is the Boltzmann constant, μ is the mean molecular weight, and m_H is the mass of a hydrogen nucleus. We include H_2 self-shielding in the same way as described above for the Enzo runs.

Figure 5 shows the gas temperature, electron fraction and H_2 fraction as a function of density computed for halo

A with Enzo (thick curves) and in the one-zone model (thin curves) for both type of UV backgrounds and for both “cool” halos (solid curves) and “hot” halos (dashed curves), with J_{21} values as indicated in the middle panels.

The results from the simulation and the one-zone model are in excellent agreement at $n \geq 10^2 \text{ cm}^{-3}$. There is a clear difference in the temperatures at $n \leq 10^2 \text{ cm}^{-3}$, which is expected, since the one-zone model prescribes a smooth adiabatic collapse, and the heating of the gas is purely due to this adiabatic compression. In contrast, in the simulation, the gas experiences shocks, which elevate the temperatures in the low-density regime. To check whether the shocks affect the comparison at higher densities, we mimicked the shocks in the one-zone model by artificially setting the temperature to $\sim 8000 \text{ K}$ at a fixed low density. We found that this makes the evolution match the simulations better at $n \leq 10^2 \text{ cm}^{-3}$, but has little effect at higher density. In particular, J_{21}^{crit} computed in the one-zone model (see below) changes by $\leq 3\%$. This is because, as already mentioned above (and will be discussed further below), J_{21}^{crit} is primarily determined by the conditions at the critical density of H_2 , which is $\sim 10^3 \text{ cm}^{-3}$.

We performed one-zone calculations similar to those shown in Figure 5, but varied J according to a Newton-Raphson scheme, until we converged on the critical value. We found $J_{21}^{\text{crit}} = 39$ for type T4 UV backgrounds, and $J_{21}^{\text{crit}} = 1.2 \times 10^4$ for type T5 backgrounds. These values fall within the range of J_{21}^{crit} identified in the Enzo runs for halo A, but are slightly below the Enzo range for halos B and C. We will discuss possibly sources of this difference below.

3.3 The importance of collisional dissociation

The one-zone model described above enables us to study the effect of each reaction on J_{21}^{crit} , thereby understanding the physics that determines J_{21}^{crit} , and identifying the uncertainty in J_{21}^{crit} due to uncertainties in the chemical reaction rates.

The five most important reactions in determining J_{21}^{crit} are (OM01): H_2 formation (reaction 10), H^- formation (reaction 9), H^- photo-dissociation (reaction 25), H_2 photo-dissociation (reaction 28) and H_2 collisional dissociation (reaction 15). Reactions 9 & 10 are the main channel of forming H_2 molecules. Reaction 25 competes with reaction 10 for H^- , modulating the effective H_2 formation rate (OM01),

$$k_{\text{form}} = k_9 \frac{k_{10}n}{k_{10}n + k_{25}}, \quad (9)$$

where k_i is the rate of reaction i (as listed in the Appendix). Both photo-dissociation and collisional dissociation compete with this effective H_2 formation process. The H_2 fraction in the gas is given approximately by the equilibrium value for whichever dissociation process dominates,

$$f_{H_2} = \min \left(\frac{k_{\text{form}}}{k_{28}} f_e n, \frac{k_{\text{form}}}{k_{15}} f_e \right). \quad (10)$$

To illustrate how these reactions determine the critical value of J_{21} , in Figures 6 and 7 we show the normalized reaction speed S as a function of n for different values of J_{21} . The normalized formation, photo-dissociation, collisional disso-

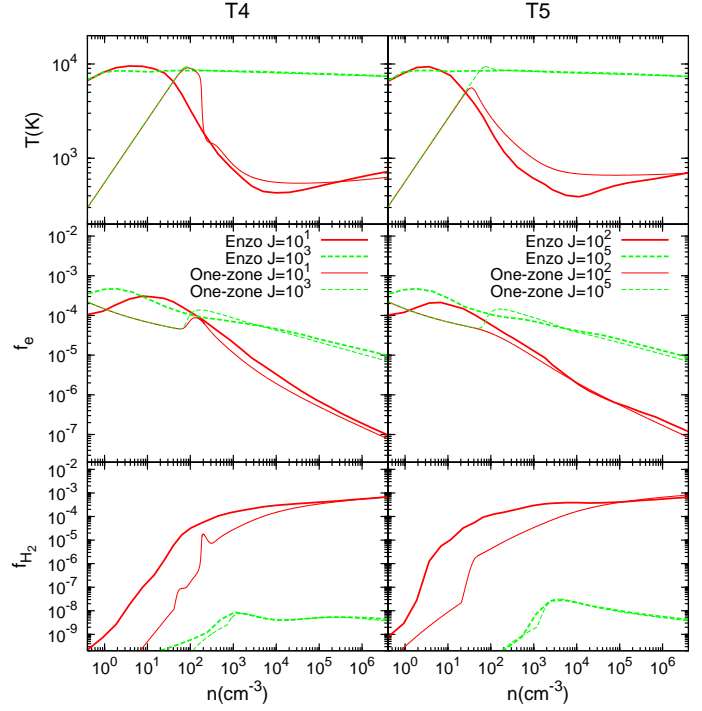


Figure 5. Gas temperature, electron fraction and H_2 fraction as a function of density computed for halo A with Enzo (thick curves) and in a one-zone model (thin curves). The solid and dashed curves show result for “cool” and “hot” halos, respectively, with the values of J_{21} as indicated in the middle panels. The left panels are for type T4 UV backgrounds, and the right panels are for type T5 UV backgrounds.

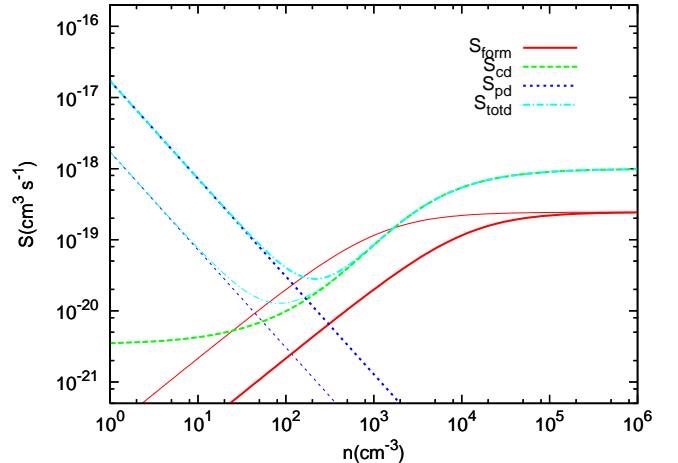


Figure 6. The normalized reaction speed S as a function of n for type T4 backgrounds. *Solid curves:* formation speed S_{form} . *Dotted curves:* photo-dissociation speed S_{pd} . *Dashed curves:* collisional dissociation speed S_{cd} . *Dash-dotted curves:* total dissociation speed S_{totd} . The thin and thick curves are for $J_{21} = 10^1$ and $J_{21} = 10^2$, respectively.

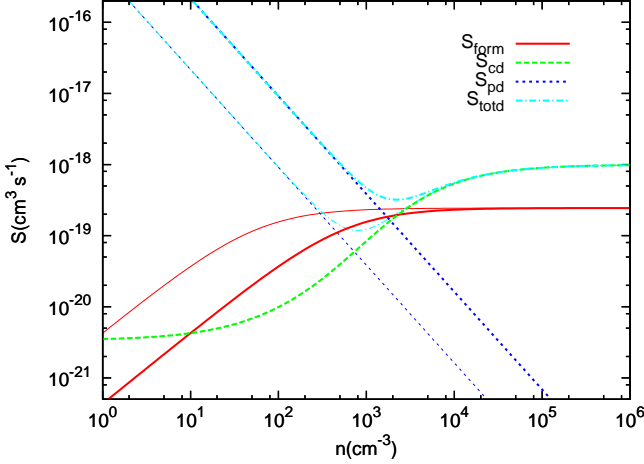


Figure 7. S as a function of n , as in Figure 6, but for type T5 backgrounds. Line types are the same as in Figure 6, except here the thin and thick curves are for $J_{21} = 10^4$ and $J_{21} = 10^5$, respectively.

ciation and total dissociation speed are defined as

$$S_{\text{form}} = k_{\text{form}} n_{\text{e}} n_{\text{H}} / n^2 \approx k_{\text{form}} f_{\text{e}}, \quad (11)$$

$$S_{\text{pd}} = k_{28} f_{\text{sh}} n_{\text{H}_2} / n^2 = k_{28} f_{\text{sh}} f_{\text{H}_2} / n, \quad (12)$$

$$S_{\text{cd}} = k_{15} n_{\text{H}_2} n_{\text{H}} / n^2 \approx k_{15} f_{\text{H}_2}, \quad (13)$$

$$S_{\text{totd}} \approx S_{\text{pd}} + S_{\text{cd}}. \quad (14)$$

In these figures, the temperature, f_{H_2} and f_{e} are set to 8000 K, 10^{-7} and 5×10^{-5} , respectively (with the self-shielding factor f_{sh} computed from equations 4 and 5). These choices were motivated by Figures 1-4, which show that f_{H_2} never exceeds $\sim 10^{-7}$ for the “hot” halos, and f_{e} is between 10^{-5} and 10^{-4} at $n \sim 10^3$. We therefore adopt 10^{-7} as the critical H_2 fraction, above which the gas could cool below ~ 8000 K.

The solid curves in Figures 6 and 7 show the formation speeds S_{form} , and the other three curves show the photo-dissociation, collisional dissociation, and total dissociation speeds, as labeled. Note that at low density, S_{form} increases with density, but at high density, it stays approximately constant. This behavior follows from equation (9): in the low density limit, $k_{10} n \ll k_{25}$, $k_{\text{form}} \approx k_9 k_{10} n / k_{25} \propto n$; whereas in the high density limit, $k_{10} n \gg k_{25}$, $k_{\text{form}} \approx k_9 \sim \text{constant}$. Likewise, the normalized dissociation rate decreases with density when it is dominated by S_{pd} , but asymptotes to a constant in the high-density limit, where collisional dissociation dominates. Figures 6 and 7 show that S_{cd} transits from a low value to a high value around the critical density $n_{\text{cr}} \sim 10^3 \text{ cm}^{-3}$.

Most importantly, the formation and dissociation speeds are both functions of J . In particular, as J is increased, the total dissociation rate is increased, but only below the density where H_2 photo-dissociation dominates collisional dissociation – the collisional rates are independent of J . Likewise, as J is increased, the effective formation rate decreases due to H^- photo-dissociation, but only at low densities, where H^- photo-dissociation is more important than collisional H^- dissociation (since, again, the collisional H^- dissociation rate is independent of J).

The critical value, J^{crit} , can be identified as the lowest

value for which the formation speed and the total dissociation speed can become equal, for any value of the density. If J is lower than this J^{crit} , then, by definition, dissociation is always more rapid than formation, and the H_2 abundance can not increase above the critical value. However, if J exceeds this J^{crit} , then at the density where $S_{\text{totd}} = S_{\text{form}}$, the H_2 abundance increases, and the gas starts to cool. Because S_{cd} drops further as the gas cools (see Fig. 8 below), more H_2 molecules are able to form, and the cooling proceeds in a runaway fashion.

Since the gas initially starts at low density, and, as shown in Figures 6 and 7, S_{totd} is high at both low and high densities, whether or not a halo would cool is mainly determined by the condition around the density n_{min} where S_{totd} reaches a minimum. The value at this minimum, $n_{\text{min}} \sim 10^2 - 10^4 \text{ cm}^{-3}$ when J_{21} is close to J^{crit} , coincides with the critical density for H_2 , $n_{\text{cr}} \approx 10^3 \text{ cm}^{-3}$ (see below).

Figures 6 and 7 also show the relative importance of H^- photo-dissociation versus direct H_2 photo-dissociation in setting the critical value of J_{21} . In particular, the J -dependence of S_{form} (solid curves) arises from H^- photo-dissociation, whereas the J -dependence of S_{totd} (dash-dotted curves) is from H_2 photo-dissociation. Comparing the thick and thin solid curves in Figures 6 and 7, we see that around the critical density of $\sim 10^3 \text{ cm}^{-3}$, H^- photo-dissociation is much more important in the T4 case. This is primarily because of the softer shape of this spectrum: for a fixed flux at 13.6 eV, the flux at $\sim 1 \text{ eV}$, just above the H^- photo-dissociation threshold, is much larger for the T4 than for the T5 case (see Omukai et al. 2008 for an explicit comparison). Interestingly, in the case of the T4 spectrum, as J is varied, the minimum in S_{totd} moves almost in parallel with the S_{form} vs. n curve. As a result, J_{21}^{crit} is, in fact, quite insensitive to the direct H_2 photo-dissociation rate (and therefore also to the details of our treatment of self-shielding). We verified this conclusion explicitly, by artificially setting $k_{28} = 0$ in the one-zone model. In this case, J_{21}^{crit} only increases by a factor of ~ 2 . The situation is very different in the case of type T5 spectrum: near the critical density, S_{form} is insensitive to J , and the critical value of J_{21} is determined almost entirely by H_2 photo-dissociation.

As mentioned above, our J_{21}^{crit} values are a factor of 3-10 lower than found by OM01 and other previous studies. The one-zone models can also be used to identify the reason for this discrepancy. In particular, we have systematically varied, one-by-one, each of the five important reaction rates enumerated above, and re-computed J_{21}^{crit} as these rates were varied. We found that the difference in J_{21}^{crit} is almost fully accounted for by the difference in our adopted H_2 collisional dissociation rate (k_{15}). In particular, when we change our k_{15} to be the same as in the one-zone calculations of OM01, but leave our other rates unchanged, we find $J_{21}^{\text{crit}} = 1.1 \times 10^3$ (for the type T4 background) and 3.4×10^4 (for the type T5 background). For the T4 case, this new J_{21}^{crit} is very close to that found by OM01. In the T5 case, our J_{21}^{crit} is still a factor of ~ 3 lower. We have varied all of the other important reaction rates (i.e., setting them to the values used in OM01), but found that this discrepancy remains. We suspect the remaining difference can be due to the different cooling functions used.

In the Enzo runs, as well as in our one-zone models,

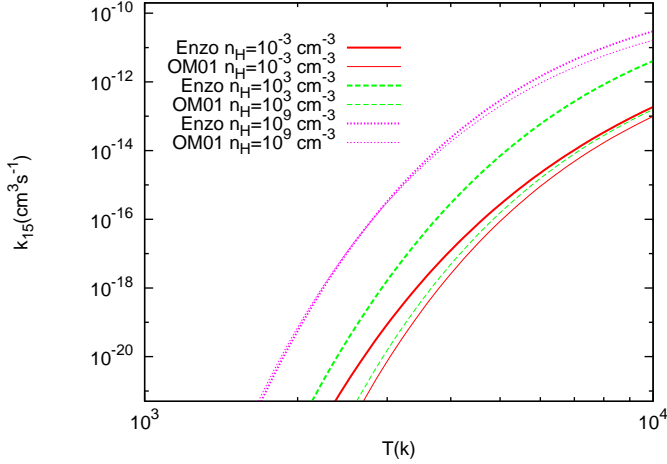


Figure 8. The H_2 collisional dissociation rate (k_{15}) adopted by Enzo and OM01, as a function of temperature, at three different densities. *Thick curves:* rates from Martin et al. (1986), used by Enzo; *Thin curves:* rates used by OM01. Solid, dashed and dotted curves show the rates at $n_H = 10^{-3}, 10^3$ and 10^9 cm^{-3} , respectively.

we adopted the H_2 collisional dissociation rate from Martin et al. (1996), while OM01 used a rate based on papers by Lepp & Shull (1983), Shapiro & Kang (1987) and Palla et al. (1983). In Figure 8, we show k_{15} used in OM01 and Enzo, as a function of temperature, for H densities of 10^{-3} cm^{-3} (low density), 10^3 cm^{-3} and 10^9 cm^{-3} (high density). As this figure shows, the rate used in Enzo is higher than the rate used in OM01, especially at the intermediate density, which is close to the critical density, and where the difference is more than a factor of 10. This large difference at the intermediate density is primarily due to the difference in n_{cr} . OM01 adopted n_{cr} from Lepp & Shull (1983), which considered only vibrational transitions. Martin et al. (1996) takes into account all rotational and vibrational-rotational transitions, and suggest that accounting for both types of transitions reduces n_{cr} by a factor of ~ 10 . This then explains and justifies the reason that our J_{21}^{crit} values are lower than in OM01.

3.4 The Origin of Scatter in J_{21}^{crit}

Another interesting result from the Enzo runs is that J_{21}^{crit} found in halos B and C are higher than both in halo A and in the one-zone model. This might be due to variations in the gas temperatures in the collapsing halos. During the assembly of the halos, due to the lack of spherical symmetry and variations in the merger histories, shocks occur at various densities and Mach numbers. This is known to cause a $\sim 20\%$ scatter in the temperature at fixed density (e.g. Loken et al. 2002). The comparison of Figures 1 and 2 with Figures 3 and 4 shows that the temperature at n_{cr} in halo A is always higher than in halo C for the J_{21} 's at which these two halos differ ($J_{21} = 10^2$ for type T4 background, $J_{21} = 3 \times 10^4$ for type T5 background). Among the five most important reactions discussed above, H_2 collisional dissociation is most sensitive to temperature. If the temperature

is lower, the collisional dissociation rate is also lower, which requires a higher J_{21}^{crit} to compensate.

We used the one-zone model (which, recall, gives good agreement with halo A) to check that this is the main reason for the different J_{21}^{crit} values for halos A and C. We find that J_{21}^{crit} indeed becomes slightly larger than 10^2 (3.2×10^4) in the case of a T4 (T5) background if the temperature is artificially decreased by $\approx 20\%$, from $\approx 8,000 \text{ K}$ to $6,000 \text{ K}$ at a density of $5 \times 10^2 \text{ cm}^{-3}$ ($5 \times 10^3 \text{ cm}^{-3}$). Note that the temperature difference occurs at a higher density in the case of a T5 background. J_{21}^{crit} could not reach 3×10^4 if we set the temperature to 6000 K at density lower than $\sim 3 \times 10^3 \text{ cm}^{-3}$. This is consistent with Figures 3 and 4, where we see that the temperature drops at larger radius (lower density) in the case of $J_{21} = 10^2$ and the T4 spectrum than in the case of $J_{21} = 3 \times 10^4$ and the T5 spectrum. Figures 6 and 7 also show that the minimum in the total dissociation rate occurs at a higher density in the case of the T5 spectrum. As Figure 8 shows, k_{15} decreases significantly – by about one order of magnitude – when the temperature is lowered to from 8000 K to 6000 K .

The H_2 formation rate (k_{10}) and the H^- formation rate (k_9) also dependent on temperature, but they work in the wrong direction to explain the increased J_{21}^{crit} for halo C: k_9 and k_{10} are lower when the temperature is lower, which would tend to reduce J_{21}^{crit} . However, the temperature dependence of k_9 and k_{10} are both much weaker than that of k_{15} . When the temperature is changed from 8000 K to 6000 K , k_9 and k_{10} decrease by 23% and 5% , respectively. We conclude that random temperature variations at the level of $\sim 20\%$, which naturally occur due to variations in the strengths of shocks that occur in the collapsing gas, can account for the scatter we observed in J_{21}^{crit} .

3.5 H_2 Self-Shielding

The value of J_{21}^{crit} is directly related to the self-shielding factor f_{sh} that we computed with an approximate method (equations 4 and 5). We here check the accuracy of these approximations a-posteriori, using the simulation outputs. We computed N_{H_2} and f_{sh} by integrating the H_2 profile from the outside in, and compared these values with those obtained from Equations 4 and 5.

We found results that were qualitatively similar in all the cases, and show only one example of such a comparison in Figure 9; for Halo A in the presence of a T5 background. The thick (thin) curves show the results from the numerical integration (approximate method). Since the halos are not spherically symmetric, integrating along different sight-lines gives different results. In our numerical integration, we first obtain a spherically average halo profile from the simulations outputs. At a given density n , we then obtain f_{sh} , by averaging the self-shielding factor, over all directions, at the radius with this density. For N_{H_2} , simple averaging makes little sense (the photodissociation rate is linearly proportional to f_{sh} , but not to N_{H_2}), so we only show the results of integrating along the single radial sight-line in the direction away from the halo center.

Figure 9 shows that over the interesting density range, N_{H_2} and f_{sh} obtained from Equations 4 and 5 agree within a factor ~ 10 , with the values obtained from the non-local integrations. In those cases when the halo gas cools, N_{H_2}

computed with the approximate method is always larger, by a factor of a few, while in those cases when the halo stays hot, N_{H_2} computed with the approximate method is larger at low density, but becomes very close to the non-local value at densities above $\geq 10^5 \text{ cm}^{-3}$. This is explained simply by the fact that Equation 5 assumes that the H_2 fraction is constant. As Figures 1 – 4 show, this is a poor assumption for “hot” halos and in the outer region of “cool” halos, where f_{H_2} decreases with radius. Only in the inner region ($R \lesssim 10 \text{ pc}$) of “cool” halos does f_{H_2} become approximately constant ($\sim 10^{-8}$). From any given location, the sightline directly pointing outward (away from the halo center) is typically the least self-shielded, and the mean non-local self-shielding factor is therefore lower than one would obtain assuming a spatially constant f_{H_2} (except close to the halo center). As a result, the thick curves in the f_{sh} panel of Figure 9 are offset downward from the positions expected from the N_{H_2} panel using Equation 4.

Since at n_{cr} , f_{H_2} computed with the approximate method is always slightly lower than its non-local value, we expect that J_{21}^{crit} would be slightly lower if f_{H_2} were computed exactly. Furthermore, self-shielding could be overestimated in our treatment, since we have ignored bulk motions of the gas. In the extreme limit where we set the H_2 self-shielding factors to zero, in the one-zone model, we find that the critical fluxes are reduced by factors of ≈ 2 and ≈ 30 , to $J_{21}^{\text{crit}} = 19$ and $J_{21}^{\text{crit}} = 440$, for the type T4 and T5 backgrounds, respectively.

4 THE MASS OF THE CENTRAL OBJECT

The thermodynamical properties of the collapsing gas have a large impact on the final object that forms in the core of the halo. An estimate for the mass of the central object, in particular, can be obtained by the following simple argument, under the assumption that the object is a single (super-)massive star. There exists a radius at which the mass accretion time-scale t_{acc} equals the Kelvin-Helmholtz time scale t_{KH} for a proto-star, with the proto-stellar mass equal to the gas mass enclosed within this radius. The gas outside this radius does not have the time to be incorporated onto the proto-star before it settles to the zero-age main sequence (ZAMS); conversely, the mass inside this radius will accrete onto the protostar before the star settles to the ZAMS (e.g. Abel et al. 2002; Omukai & Palla 2003; O’Shea & Norman 2007). While this argument ignores various feedback processes that can occur and affect the final stellar mass, it gives a useful order-of-magnitude estimate. See McKee & Tan (2008) for a more detailed discussion in the context of first star formation in minihalos.

In Figures 10 and 11, we show the accretion time scale $t_{\text{acc}} \equiv R/\langle v_R \rangle$ as a function of the gas mass M_{gas} enclosed within a sphere of radius R . Here $\langle v_R \rangle$ is the mean radial in-fall velocity at R . These figures show that at enclosed masses of $< 10^6 M_{\odot}$, the accretion rates in the “hot” halos are 1-2 orders of magnitude higher than for the “cool” halos. The Kelvin-Helmholtz contraction time scale for metal-free stars is approximately 10^5 years, with a relatively weak dependence on the proto-stellar mass (Schaerer 2002). Within this time, the central object in a “hot” halo will accumulate $10^5 M_{\odot}$, while the object in a “cool” halo could accumulate

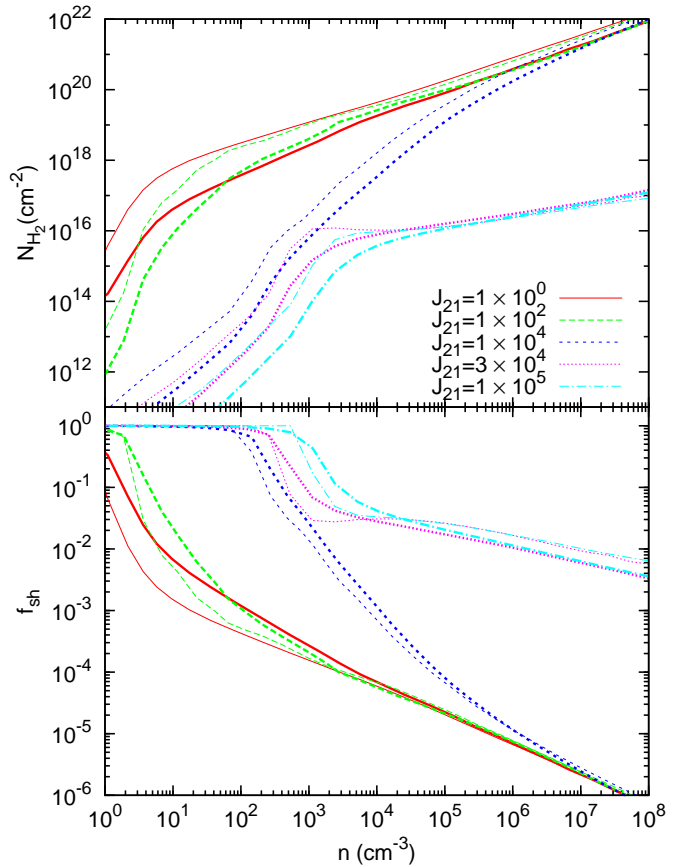


Figure 9. The H_2 column density and self-shielding factor in the Lyman–Werner bands for Halo A and a T5 background. The *thin* curves were computed from the approximations in Equations 4 and 5; the *thick* curves were obtained by numerically integrating the H_2 profile in the simulations. The various line types correspond to different intensities J , as labeled. See text for details.

$10^2 - 10^4 M_{\odot}$. The latter values are very similar to previous estimates for the masses of the first stars that form in minihalos (Abel et al. 2002; Bromm et al. 2002; O’Shea & Norman 2007); this is not surprising, given that the densities and temperatures reached in these “cool” halos via efficient H_2 -cooling are very similar to those in lower-mass minihalos. However, the value $10^5 M_{\odot}$ for the “hot” halos is much larger; in particular, a supermassive, metal-free star with this large a mass suffers from post-Newtonian instabilities, and ultimately collapses without an explosion to produce a SMBH of the same mass (Fuller, Woosley & Weaver 1986).

Given that the effect of the UV background is to dissociate molecules, and to reduce the efficiency of cooling, it may be surprising that the gas accretion rate in the “hot” halos is higher than in the “cool” halos, whose gas cools more efficiently. However, we note that the accretion rates in Figure 10 and 11 are shown at different times: although the gas collapse in the “hot” halos is more rapid, it occurs after a significant delay. Once the collapse begins, it proceeds

over the dynamical time scale,

$$t_{\text{acc}} \sim t_{\text{ff}} = \sqrt{\frac{3\pi}{32G\rho}}. \quad (15)$$

Here, G is the gravitational constant, and ρ is the total (gas + dark matter) density. On the other hand, the infall speed is modulated by the sound speed. Once the infall becomes supersonic, weak shocks occur, which tend to slow the infall. These shocks also provide an additional source of heating the gas, thereby elevating the sound speed. As a result, the sound speed and the infall speed tend to trace each other. In Figure 12, we show spherically averaged profiles of the radial velocity (solid curves) and the sound speed (dashed curves) in halo A (and type T4 backgrounds). The thick and thin curves are for $J_{21} = 10^1$ and $J_{21} = 10^3$, respectively. Although not exactly equal, the sound speed and the radial infall speed are always of the same. A similar conclusion could be drawn from Figure 13, where we show three time scales: the cooling time (solid curves), the sound crossing time (defined as R/c_s ; dashed curves) and the free-fall time (dotted curves). The thick and thin curves are for the same two values of J_{21} as in Figure 12. Inside the virial radius (i.e., within a few pc, where the gas is first shocked and heated to 10^4K) the cooling and sound crossing times both trace the free-fall time scale to within a factor of ~ 2 . It is particularly revealing that the good match between the three time-scales holds over a factor of ~ 300 in radii. Using the condition that the sound crossing time equals the free-fall time,

$$R/c_{\text{sound}} = R\sqrt{\frac{\mu m_H}{\gamma kT}} \approx \sqrt{\frac{3\pi}{32G\rho}}, \quad (16)$$

together with $M \sim \rho R^3$ to convert ρ in Equation 15 to M and T , we find

$$t_{\text{accr}} \approx t_{\text{ff}} \approx GM \left(\frac{\mu m_H}{\gamma kT} \right)^{3/2} = \frac{GM}{c_{\text{sound}}^3}, \quad (17)$$

where a numerical factor of order unity (which depends on the actual density profile) has been omitted. Note that to within these factors, this result agrees with the well-known result for the accretion time-scale in the self-similar collapse of a singular isothermal sphere (Shu 1977). In their simulations, O'Shea & Norman (2007) find the same scaling of the accretion rate with sound-speed, and attribute this scaling to the physics of the collapsing isothermal sphere; note that our explanation – namely that weak shocks limit the infall velocity to be close to the sound speed – is somewhat different. Equation 17 predicts a linear dependence between t_{accr} and the enclosed mass M , as well as $t_{\text{acc}} \propto T^{-3/2}$; both of these scalings are in good agreement with the accretion times shown in Figures 10 and 11. As discussed in § 3 above, the central gas temperatures in the “hot” halos are a factor of ~ 6 higher than those in the “cool” halos (with the exception of the runs with $J_{21} \leq 1$). Based on the above argument, t_{acc} is therefore expected to be a factor of ~ 15 smaller, at a given M_{gas} , for the “hot” halos. This factor is indeed in good agreement with the difference in the accretion rates for the two types of halos shown in Figures 10 and 11.

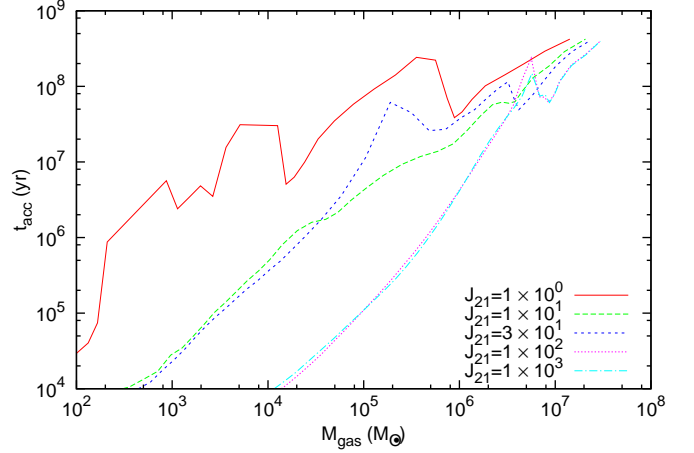


Figure 10. The local accretion time-scale t_{acc} as a function of the enclosed gas mass M_{gas} for Halo A and a T4 background with different intensities, as labeled.

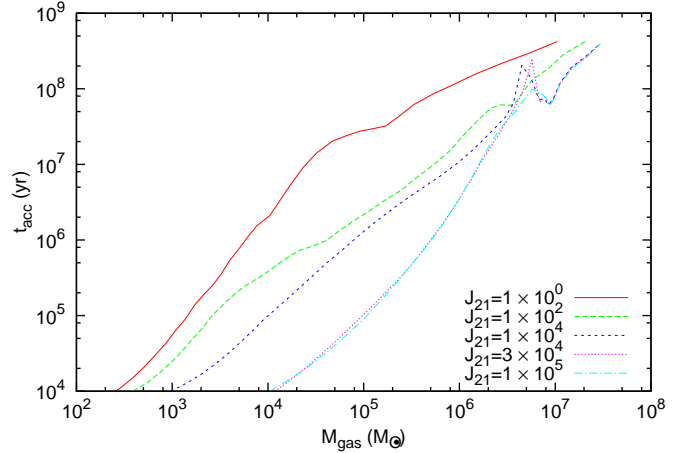


Figure 11. Same as Figure 10 except for type T5 backgrounds.

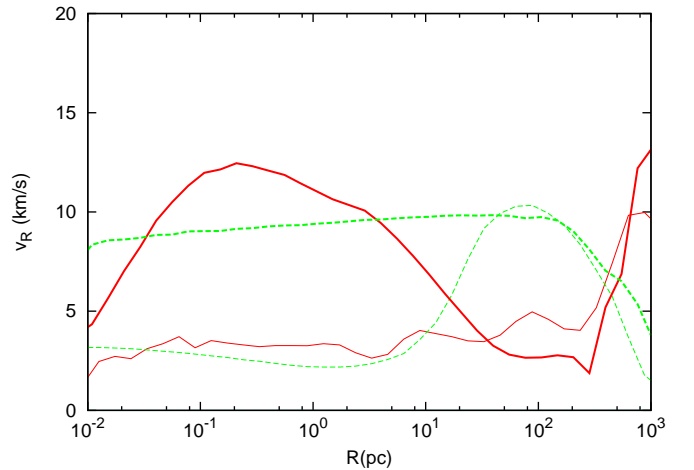


Figure 12. The radial velocity (solid curves) and sound speed (dashed curves) as a function of radius in halo A in the presence of type T4 backgrounds. The thick and thin curves are for $J_{21} = 10^1$ and 10^3 , respectively.

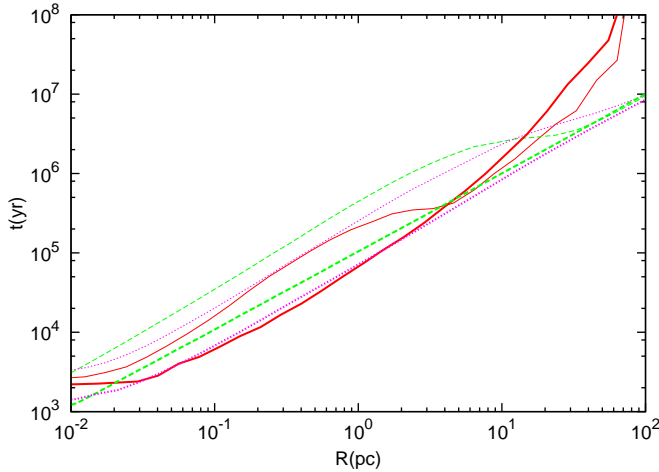


Figure 13. The cooling (solid curves), sound-crossing (dashed curves) and free-fall time scale (dotted curves) as a function of radius in halo A, in the presence of type T4 backgrounds. The thick and thin curves are for $J_{21} = 10^1$ and 10^3 , respectively.

5 CONCLUSIONS

By performing a series of simulations with the AMR code Enzo, we determined the critical intensity of the UV background needed to suppress the H_2 cooling in dark matter halos with virial temperatures of $T_{\text{vir}} \gtrsim 10^4 \text{ K}$. We have modified Enzo to include H^- photo-dissociation, as well as self-shielding of H_2 in the Lyman–Werner bands. To increase the computing speed, the self-shielding effect was calculated with an approximate method that uses only local physical quantities; we have shown, however, that this simple approximation is accurate to better than an order of magnitude.

In agreement with earlier results from a one-zone model (OM01), we found that, depending on whether the background intensity is above or below the critical value, the halos can be unambiguously grouped into two categories: “hot” halos and “cool” halos. In general, “hot” halos have much higher central gas temperature, density, and electron fraction and a much lower H_2 fraction. In the “cool” halos, the temperature drops inside $R \sim 10 \text{ pc}$, which corresponds to a local density $n \sim 10^3 \text{ cm}^{-3}$.

For type T4 (T5) spectra, J_{21}^{crit} is found to be in the range of $3 \times 10^1 - 10^2$ ($10^4 - 3 \times 10^4$) for halo A, and $10^2 - 2 \times 10^2$ ($3 \times 10^4 - 10^5$) for halos B and C. These values show that the critical flux varies significantly from halo to halo; we attribute this variation to scatter in temperature at a given density. Most importantly, the values of J_{21}^{crit} we find are a factor of 3–10 lower than previously estimated. Using one-zone models with simplified dynamics, we studied the dependence of J_{21}^{crit} on each of the important reaction rates. We have shown that the difference between our results and previous estimates can be attributed to our adoption of a different, more accurate, H_2 collisional dissociation rate.

In those halos in which H_2 cooling is suppressed, the gas cools efficiently, but remains relatively hot, at a temperature near $T \sim 8000 \text{ K}$. While gas collapse starts with a significant delay, we have shown that, as a result of the elevated temperature, the gas accretion rate in these halos is ultimately increased by $\approx 1 - 2$ orders of magnitude. As a result, a supermassive star with a mass of $10^5 M_\odot$ may

form in the cores of these halos (compared to $10^{2-3} M_\odot$ stars in the presence of H_2 cooling), ultimately producing a supermassive black hole (SMBH) with a comparable mass.

The critical UV fluxes required to suppress H_2 cooling in halos with $T_{\text{vir}} \gtrsim 10^4 \text{ K}$ are high compared to the expected level of the cosmic UV background at high redshifts. Most likely, the halos exposed to a super-critical UV flux are a small subset of all $T_{\text{vir}} \gtrsim 10^4 \text{ K}$ halos that happen to sample the bright-end tail of the fluctuating cosmic UV background. This makes the reductions in J_{21}^{crit} that we have found particularly significant: according to a model for the fluctuating UV background, as sampled by DM halos (Dijkstra et al. 2008) the 10-fold decrease in J^{crit} can increase the number of candidate DM halos, where direct SMBH formation may be feasible, by a factor of $\approx 10^3$.

ACKNOWLEDGMENTS

This work was supported by the NSF grant AST-05-07161. ZH acknowledges support by the Polányi Program of the Hungarian National Office of Technology. GB acknowledges support from NSF grants AST-05-07161, AST-05-47823, and AST-06-06959, as well as computational resources from the National Center for Supercomputing Applications.

REFERENCES

- Abel, T., Anninos, P., Zhang, Y., & Norman, M. L. 1997, *NewA*, 2, 181
- Abel, T., Bryan, G. L., Norman, M. L. 2000, *ApJ*, 540, 39
- Abel, T., Bryan, G. L., Norman, M. L. 2002, *Science*, 295, 93
- Alvarez, M.A., Wise, J.H., Abel, T. 2009, *ApJL* submitted, arXiv.org:0811.0820
- Baker, J.G., Centrella, J.; Choi, D.; Koppitz, M., & van Meter, J. 2006, *Phys. Rev. Lett.* 96, 111102
- Begelman, M., Volonteri, M., & Rees, M. J. 2006, *MNRAS*, 370, 289
- Berger, M. J., & Colella, P. 1989, *J. Comput. Phys.*, 82, 64
- Blecha, L. & Loeb, A. 2008, *MNRAS*, 390, 1311
- Bromley, J.M., Somerville, R.S., & Fabian, A.C. 2004, *MNRAS* 350, 456
- Bromm, V., Coppi, P. S., Larson, R. B. 2002, *ApJ*, 564, 23
- Bromm, V., Kudritzki, R. P., & Loeb, A. 2001, *ApJ*, 552, 464
- Bromm, V., & Loeb, A. 2003, *ApJ*, 596, 34 (BL03)
- Bryan, G. L., 1999, *Comput. Sci. Eng.*, 1, 46
- Campanelli, M., Lousto, C., Marronetti, P., & Zlochower, Y. 2006, *Phys. Rev. Lett.* 96, 111101
- Ciotti, L., & Ostriker, J. P. 2001, *ApJ*, 551, 131
- Ciotti, L., & Ostriker, J. P. 2007, *ApJ*, 665, 1038
- Dijkstra, M., Haiman, Z., Rees, M. J., & Weinberg, D. H. 2004, *ApJ*, 601, 666
- Dijkstra, M., Haiman, Z., Mesinger, A., & Wyithe, S. 2008, *MNRAS*, 391, 1961
- Eisenstein, D.J., & Hut, P. 1998, *ApJ*, 498, 137
- Fan, X. 2006 *NewA Rev.*, 50, 665
- Fuller, G. M., Woosley, S. E., & Weaver, T. A. 1986, *ApJ*, 307, 675
- Galli, D., & Palla, F. 1998, *A&A*, 335, 403
- Haiman, Z. 2004, *ApJ*, 613, 36

Haiman, Z., Rees, M. J., & Loeb, A. 1997, *ApJ*, 484, 985
 Komatsu et al. 2009, *ApJS*, 180, 330
 Koushiappas, S. M., Bullock, J. S., & Dekel, A. 2004, *MNRAS*, 354, 292
 Lepp, S. & Shull, J. M. 1983, *ApJ*, 270, 578
 Lodato, G., & Natarajan, P. 2006, *MNRAS*, 371, 1813
 Lodato, G., & Natarajan, P. 2007, *MNRAS*, 377, 64
 Loken, C., Norman, M.L., Nelson, E., Burns, J., Bryan, G.L., & Motl, P. 2002, *ApJ*, 579, 571
 Machacek, M. E., Bryan, G. L., & Abel, T. 2001, *ApJ*, 548, 509
 Machacek, M. E., Bryan, G. L., & Abel, T. 2003, *MNRAS*, 338, 273
 Martin, P. G., Schwarz, D. H., & Mandy, M. E. 1996, *ApJ*, 461, 265
 McKee, C.F., & Tan, J.F. 2008, *ApJ*, 681, 771
 Mesinger, A., Bryan, G. L., & Haiman, Z. 2006, *ApJ*, 648, 835
 Mesinger, A., Bryan, G. L., & Haiman, Z. 2008, *ApJ*, submitted, arXiv.org:0812.2479
 McGreer, I. D., & Bryan, G. L. 2008, *ApJ*, 685, 8
 Milosavljević, M., Bromm, V., Couch, S. M., & Oh, S. P. 2009a, *ApJ*, 698, 766
 Milosavljević, M., Couch, S. M., & Bromm, V. 2009b, *ApJ*, 696, L146
 Molnar, S. M., Hearn, N., Haiman, Z., Bryan, G., Evrard, A. E., & Lake, G. 2009, *ApJ*, 696, 1640
 Norman M. L. & Bryan G. L., 1999, in Miyama S. M., Tomisaka K., Hanawa K., eds, *Astrophys. Sci. Sci. Library* Vol. 240, Numerical Astrophysics, Kluwer, Boston, p. 19
 Oh, S. P., & Haiman, Z. 2002, *ApJ*, 569, 558 (OH02)
 Omukai, K., & Palla, F. 2003, *ApJ*, 589, 677
 O'Shea, B.W., Norman, M. L., 2008, *ApJ*, 673, 14
 O'Shea, B.W., Norman, M. L., 2007, *ApJ* 654, 66
 Omukai, K. 2001, *ApJ*, 546, 635 (OM01)
 Omukai, K., Schneider, R., & Haiman, Z. 2008, *ApJ*, 686, 801
 Omukai, K. & Yoshii, Y. 2003, *ApJ*, 599, 746
 O'Shea, B., Bryan, G., Bordner, J., Norman, M., Abel, T., Harkness, R., & Kritsuk, A. 2004, in *Adaptive Mesh Refinement: Theory and Applications*, ed. T. Plewa, T. Linde, & G. Weirs (Berlin: Springer), 343
 Palla, F., Salpeter, E. E., & Stahler, S. W. 1983, *ApJ*, 271, 632
 Pretorius, F. 2005, *Phys. Rev. Lett.* 95, 121101
 Regan, J. A., & Haehnelt, M. G. 2009a, *MNRAS*, 393, 858
 Regan, J. A., & Haehnelt, M. G. 2009a, *MNRAS*, 396, 343
 Richards, G., et al. 2004, *AJ*, 127, 1305
 Schaerer, D. 2002, *A&A*, 382, 28
 Shapiro, P. R., & Kang, H. 1987, *ApJ*, 318, 32
 Spaans, M., & Silk, J. 2006, *ApJ*, 652, 902
 Shu, F. H. 1977, *ApJ*, 214, 488
 Tanaka, T., & Haiman, Z. 2009, *ApJ*, 696, 1798
 Tumlinson, J., & Shull, M. J. 2000, *ApJ*, 528, L65
 Turner, E. L. 1991, *AJ*, 101, 5
 Volonteri, M., & Rees, M. J. 2005, *ApJ*, 633, 624
 Volonteri, M., & Rees, M. J. 2006, *ApJ*, 650, 669
 Volonteri, M., Lodato, G. & Natarajan, P. 2008, *MNRAS*, 383, 1079
 Willott, C. J., McLure, R. J., & Jarvis, M. J. 2003, *ApJ*, 587, 15
 Wise, J.H., Abel, T. 2007, *ApJ*, 671, 1559

Yoo, J., & Miralda-Escudé, J. 2004, *ApJ*, 614, 25

Reaction	Rate Coefficient k ($\text{cm}^3 \text{s}^{-1}$) or Cross-section σ (cm^2)
(1) $\text{H} + \text{e}^- \rightarrow \text{H}^+ + 2\text{e}^-$	$k_1 = \exp(-32.71396786375$ $+13.53655609057(\ln T_{\text{eV}})$ $-5.739328757388(\ln T_{\text{eV}})^2$ $+1.563154982022(\ln T_{\text{eV}})^3$ $-0.2877056004391(\ln T_{\text{eV}})^4$ $+0.03482559773736999(\ln T_{\text{eV}})^5$ $-0.00263197617559(\ln T_{\text{eV}})^6$ $+0.0001119543953861(\ln T_{\text{eV}})^7$ $-2.039149852002 \times 10^{-6}(\ln T_{\text{eV}})^8)$
(2) $\text{He} + \text{e}^- \rightarrow \text{He}^+ + 2\text{e}^-$	$k_2 = \exp(-44.09864886561001$ $+23.91596563469(\ln T_{\text{eV}})$ $-10.75323019821(\ln T_{\text{eV}})^2$ $+3.058038757198(\ln T_{\text{eV}})^3$ $-0.5685118909884001(\ln T_{\text{eV}})^4$ $+0.06795391233790001(\ln T_{\text{eV}})^5$ $-0.005009056101857001(\ln T_{\text{eV}})^6$ $+0.0002067236157507(\ln T_{\text{eV}})^7$ $-3.649161410833 \times 10^{-6}(\ln T_{\text{eV}})^8)$
(3) $\text{He}^+ + \text{e}^- \rightarrow \text{He}^{++} + 2\text{e}^-$	$k_3 = \exp(-68.71040990212001$ $+43.93347632635(\ln T_{\text{eV}})$ $-18.48066993568(\ln T_{\text{eV}})^2$ $+4.701626486759002(\ln T_{\text{eV}})^3$ $-0.7692466334492(\ln T_{\text{eV}})^4$ $+0.08113042097303(\ln T_{\text{eV}})^5$ $-0.005324020628287001(\ln T_{\text{eV}})^6$ $+0.0001975705312221(\ln T_{\text{eV}})^7$ $-3.165581065665 \times 10^{-6}(\ln T_{\text{eV}})^8)$
(4) $\text{H}^+ + \text{e}^- \rightarrow \text{H} + \text{h}\nu$	$k_4 = \exp(-28.61303380689232$ $-0.7241125657826851(\ln T_{\text{eV}})$ $-0.02026044731984691(\ln T_{\text{eV}})^2$ $-0.002380861877349834(\ln T_{\text{eV}})^3$ $-0.0003212605213188796(\ln T_{\text{eV}})^4$ $-0.00001421502914054107(\ln T_{\text{eV}})^5$ $+4.989108920299513 \times 10^{-6}(\ln T_{\text{eV}})^6$ $+5.755614137575758 \times 10^{-7}(\ln T_{\text{eV}})^7$ $-1.856767039775261 \times 10^{-8}(\ln T_{\text{eV}})^8$ $-3.071135243196595 \times 10^{-9}(\ln T_{\text{eV}})^9)$
(5) $\text{He}^+ + \text{e}^- \rightarrow \text{He} + \text{h}\nu$	$k_5 = 1.54 \times 10^{-9}(1 + 0.3/\exp(8.099328789667/T_{\text{eV}}))$ $/(\exp(40.49664394833662/T_{\text{eV}}) \times T_{\text{eV}}^{1.5})$ $+3.92 \times 10^{-13}/T_{\text{eV}}^{0.6353}$
(6) $\text{He}^{++} + \text{e}^- \rightarrow \text{He}^+ + \text{h}\nu$	$k_6 = 3.36 \times 10^{-10} T^{-\frac{1}{2}} (T/1000)^{-0.2} (1 + (T \times 10^{-6})^{0.7})^{-1}$
(7) $\text{H} + \text{H}^+ \rightarrow \text{H}_2^+ + \text{h}\nu$	$k_7 = 1.85 \times 10^{-23} \times T^{1.8}$ $k_7 = 5.81 \times 10^{-16} (T/56200)^{(-0.6657 \log(T/56200))}$
	$T \leq 6.7 \times 10^3 \text{ K}$ $T > 6.7 \times 10^3 \text{ K}$

APPENDIX: REACTION RATES AND CROSS SECTIONS

T and T_{eV} are the gas temperature in units of K and eV, respectively.

Reaction	Rate Coefficient k ($\text{cm}^3 \text{s}^{-1}$) or Cross-section σ (cm^2)	
(8) $\text{H}_2^+ + \text{H} \rightarrow \text{H}_2 + \text{H}^+$	6.0×10^{-10}	
(9) $\text{H} + \text{e}^- \rightarrow \text{H}^- + h\nu$	$k_9 = 6.775 \times 10^{-15} T_{\text{eV}}^{0.8779}$	
(10) $\text{H} + \text{H}^- \rightarrow \text{H}_2 + \text{e}^-$	$k_{10} = 1.43 \times 10^{-9}$	$T_{\text{eV}} \leq 0.1$
	$k_{10} = \exp(-20.06913897587003$	$T_{\text{eV}} > 0.1$
	$+0.2289800603272916(\ln T_{\text{eV}})$	
	$+0.03599837721023835(\ln T_{\text{eV}})^2$	
	$-0.004555120027032095(\ln T_{\text{eV}})^3$	
	$-0.0003105115447124016(\ln T_{\text{eV}})^4$	
	$+0.0001073294010367247(\ln T_{\text{eV}})^5$	
	$-8.36671960467864 \times 10^{-6}(\ln T_{\text{eV}})^6$	
	$+2.238306228891639 \times 10^{-7}(\ln T_{\text{eV}})^7)$	
(11) $\text{H}_2^+ + \text{e}^- \rightarrow 2\text{H}$	$k_{11} = 1.0 \times 10^{-8}$	$T \leq 617 \text{ K}$
	$k_{11} = 1.32 \times 10^{-6} T^{-0.76}$	$T > 617 \text{ K}$
(12) $\text{H}_2^+ + \text{H}^- \rightarrow \text{H}_2 + \text{H}$	$k_{12} = 5.00 \times 10^{-6} T^{-\frac{1}{2}}$	
(13) $\text{H}^- + \text{H}^+ \rightarrow 2\text{H}$	$k_{13} = 6.5 \times 10^{-9} T_{\text{eV}}^{-\frac{1}{2}}$	
(14) $\text{H}_2 + \text{e}^- \rightarrow \text{H} + \text{H}^-$	$k_{14} = 0.0$ (not used in Enzo)	
(15) $\text{H}_2 + \text{H} \rightarrow 3\text{H}$	see expression in Martin et al. (1996)	
(16) $\text{H}_2 + \text{H}_2 \rightarrow \text{H}_2 + 2\text{H}$	$k_{16} = 0.0$ (not used in Enzo)	
(17) $\text{H}_2 + \text{H}^+ \rightarrow \text{H}_2^+ + \text{H}$	$k_{17} = \exp(-24.24914687731536$	
	$+3.400824447095291(\ln T_{\text{eV}})$	
	$-3.898003964650152(\ln T_{\text{eV}})^2$	
	$+2.045587822403071(\ln T_{\text{eV}})^3$	
	$-0.5416182856220388(\ln T_{\text{eV}})^4$	
	$+0.0841077503763412(\ln T_{\text{eV}})^5$	
	$-0.007879026154483455(\ln T_{\text{eV}})^6$	
	$+0.0004138398421504563(\ln T_{\text{eV}})^7$	
	$-9.36345888928611 \times 10^{-6}(\ln T_{\text{eV}})^8)$	
(18) $\text{H}_2 + \text{e}^- \rightarrow 2\text{H} + \text{e}^-$	$k_{18} = 5.6 \times 10^{-11} \exp(-102124/T) T^{0.5}$	
(19) $\text{H}^- + \text{e}^- \rightarrow \text{H} + 2\text{e}^-$	$k_{19} = \exp(-18.01849334273$	
	$+2.360852208681(\ln T_{\text{eV}})$	
	$-0.2827443061704(\ln T_{\text{eV}})^2$	
	$+0.01623316639567(\ln T_{\text{eV}})^3$	
	$-0.03365012031362999(\ln T_{\text{eV}})^4$	
	$+0.01178329782711(\ln T_{\text{eV}})^5$	
	$-0.001656194699504(\ln T_{\text{eV}})^6$	
	$+0.0001068275202678(\ln T_{\text{eV}})^7$	
	$-2.631285809207 \times 10^{-6}(\ln T_{\text{eV}})^8)$	
(20) $\text{H}^- + \text{H} \rightarrow 2\text{H} + \text{e}^-$	$k_{20} = 2.56 \times 10^{-9} T_{\text{eV}}^{1.78186}$	$T_{\text{eV}} \leq 0.1$
	$k_{20} = \exp(-20.37260896533324$	$T_{\text{eV}} > 0.1$
	$+1.139449335841631(\ln T_{\text{eV}})$	
	$-0.1421013521554148(\ln T_{\text{eV}})^2$	
	$+0.00846445538663(\ln T_{\text{eV}})^3$	
	$-0.0014327641212992(\ln T_{\text{eV}})^4$	
	$+0.0002012250284791(\ln T_{\text{eV}})^5$	
	$+0.0000866396324309(\ln T_{\text{eV}})^6$	
	$-0.00002585009680264(\ln T_{\text{eV}})^7$	
	$+2.4555011970392 \times 10^{-6}(\ln T_{\text{eV}})^8$	
	$-8.06838246118 \times 10^{-8}(\ln T_{\text{eV}})^9)$	
(21) $\text{H}^- + \text{H}^+ \rightarrow \text{H}_2^+ + \text{e}^-$	$k_{21} = 4 \times 10^{-4} T^{-1.4} \exp(-15100/T)$	$T \leq 10^4 \text{ K}$
	$k_{21} = 1 \times 10^{-8} T^{-0.4}$	$T > 10^4 \text{ K}$
(22) $\text{H} + h\nu \rightarrow \text{H}^+ + \text{e}^-$	$\sigma_{22} = 6.3 \times 10^{-18} (\frac{13.6\text{eV}}{h\nu})^4 \exp(4 - 4(\tan^{-1}\epsilon/\epsilon)/[1 - \exp(-2\pi/\epsilon)]$	
(23) $\text{He} + h\nu \rightarrow \text{He}^+ + \text{e}^-$	$\sigma_{23} = 0.694 \times 10^{-18} [(\frac{h\nu}{\text{eV}})^{1.82} + (\frac{h\nu}{\text{eV}})^{3.23}]^{-1}$	
(24) $\text{He}^+ + h\nu \rightarrow \text{He}^{++} + \text{e}^-$	$\sigma_{24} = 1.575 \times 10^{-18} (\frac{54.4\text{eV}}{h\nu})^4 \exp(4 - 4(\tan^{-1}\epsilon/\epsilon)/[1 - \exp(-2\pi/\epsilon)]$	
(25) $\text{H}^- + h\nu \rightarrow \text{H} + \text{e}^-$	$k_{25} = 10^{-10} \alpha J_{21}$; $\alpha = 2000$ for T4 spectrum, 0.1 for T5 spectrum	
(26) $\text{H}_2^+ + h\nu \rightarrow \text{H} + \text{H}^+$	see expression in Shapiro & Kang (1987)	
(27) $\text{H}_2 + h\nu \rightarrow \text{H}_2^+ + \text{e}^-$	see expression in Shapiro & Kang (1987)	
(28) $\text{H}_2 + h\nu \rightarrow 2\text{H}$	$k_{28} = 10^{-12} \beta J_{21}$; $\beta = 3$ for T4 spectrum, 0.9 for T5 spectrum	